

Use of Remote Sensing to Detect Soybean Cyst Nematode-Induced Plant Stress¹

F. W. NUTTER, JR.,² G. L. TYLKA,³ J. GUAN,⁴ A. J. D. MOREIRA,⁵ C. C. MARETT,⁶ T. R. ROSBURG,⁷ J. P. BASART,⁸
AND C. S. CHONG⁹

Abstract: Integrating remote sensing and geographic information systems (GIS) technologies offers tremendous opportunities for farmers to more cost effectively manage the causes of crop stress. Initial soybean cyst nematode (SCN) population densities from 995 2×3-m quadrats were obtained from a soybean field near Ames, Iowa, in 2000. The percentage of sunlight reflected from each quadrat was measured weekly using a multispectral radiometer beginning in mid-May and continuing through mid-September. Aerial images were obtained at heights above the field ranging from 45 to 425 m on 12 dates during the soybean growing season. This was accomplished using color film and infrared film in conjunction with a filter to measure reflectance in the near-infrared region (810 nm). Satellite images (Landsat 7) were obtained for five dates during the 2000 growing season. Maps depicting initial SCN population densities, soybean yield, soy oil, and soy protein were generated using the GIS software program ArcView. Percentage reflectance (810 nm), aerial image intensity, and satellite image intensity data then were regressed against soybean yield, soy oil, and soy protein concentrations obtained from each geospatially referenced soybean quadrat. Percentage reflectance measurements explained up to 60% of the variation in initial SCN population densities within soybean quadrats and up to 91% of the variation in soybean yield. Aerial image and satellite image intensities explained up to 80% and 47% of the variation in soybean yield, respectively. Percentage reflectance data also explained 36% and 54% of the variation in oil and protein concentrations of the harvested soybeans, respectively. These results indicate that remote sensing coupled with GIS technologies may provide new tools to detect and quantify SCN population densities and their impacts on the quantity and quality of soybean yield.

Key words: detection, *Heterodera glycines*, nematode, management, plant disease losses, remote sensing, soybean cyst nematode.

The soybean cyst nematode (SCN), *Heterodera glycines* Ichinohe, is a serious and widespread pathogen of soybeans throughout the United States. Results of a random survey of six major soybean-producing states in the Midwest in 1995–1996 indicated that *H. glycines* was present in 46% to 83% of the fields tested (Workneh et al., 1999). Unfortunately, many growers do not realize that their fields are infested with the nematode until *H. glycines* population densities reach population densities that result in clearly visible aboveground symptoms. Even when soybean producers are aware that their fields are infested with SCN, they usually do not know the extent of SCN infestation and amount of yield loss being caused by this pest.

One of the basic tenets of precision agriculture is that the presence, distribution, and intensity of any yield-reducing factor (or factors) within fields must be

known. Yet, as indicated above, soybean producers rarely know exactly where (among and within soybean fields) *H. glycines* is a yield-limiting problem. To obtain such knowledge, one must collect soil samples within fields using a systematic grid of quadrats and then have these samples analyzed to determine the presence and population density of the nematode. Unfortunately, collection and processing of soil samples are both labor intensive and cost prohibitive.

The primary reason that the presence of *H. glycines* within soybean fields often is not realized before yield losses are incurred is because it may take several years for the nematode to reach population densities that result in visible, aboveground symptoms. At lower population densities, aggregated patches of stunted plants may be visible in the field. These patches are round to oval in shape and are not easily observed by scouts walking the fields, yet soybean yield is being adversely affected. Rows of soybeans grown on *H. glycines*-infested land can be slow to close or fill in with foliage compared to noninfested rows, thus creating greater weed problems in SCN-infested areas of the field. At higher *H. glycines* population densities, patches of various sizes within soybean fields are chlorotic and severely stunted. The stunting of plants and the slower rate of plant growth both result in reductions in healthy (green) leaf area index (GLAI). Leaf area per unit ground area has been used to describe and explain the relationship between canopy development and yield (Faivre and Fischer, 1996; Guan and Nutter, 2000; Jackson et al., 1980). Differences in GLAI in fields are extremely difficult to visually detect and labor-intensive to quantify at ground level (Nutter et al., 1999). However, *H. glycines*-infested patches should be clearly obvious using remote sensing and geographic information systems (GIS) technologies that can accurately and precisely measure and map variations in GLAI as well as

Received for publication 14 September 2001.

Paper delivered in a symposium on Application of GIS and GPS Precision Agriculture Technologies in Nematology and Plant Pathology, Society of Nematologists Annual Meeting, 24–29 August 2001, Salt Lake City, UT

¹ Supported by grants from the Iowa Space Grant Consortium, the North Central Soybean Research Program, and the Iowa Soybean Promotion Board. This research was also supported, in part, from funds allocated by the Iowa Agriculture and Home Economics Experiment Station. Publication No. J-19541, Project No. 3394 and 3288.

² Epidemiologist, Professor, and Project Leader, Department of Plant Pathology, Iowa State University, Ames, IA 50011.

³ Nematologist and Professor, Department of Plant Pathology, Iowa State University, Ames, IA 50011.

⁴ Research Associate, Epidemiology, Department of Plant Pathology, Iowa State University, Ames, IA 50011.

⁵ Graduate Assistant, Department of Plant Pathology, Iowa State University, Ames, IA 50011.

⁶ Assistant Scientist, Nematology, Department of Plant Pathology, Iowa State University, Ames, IA 50011.

⁷ Associate Professor, Department of Biology, Drake University, Des Moines, IA 50311.

⁸ Professor, Department of Electrical and Computer Engineering, Iowa State University, Ames, IA 50011.

⁹ Graduate Assistant, Department of Electrical and Computer Engineering, Iowa State University, Ames, IA 50011.

E-mail: fwn@iastate.edu

This paper was edited by B. C. Hyman.

yield, protein, and oil concentrations over time and space (Adcock et al., 1990; Guan and Nutter, 2000; Nutter, 1989; Nutter et al., 2000).

Epidemiological principles can be employed to generate a wide range of biotic and abiotic stress intensities over time and space (Nutter and Gaunt, 1996). Because yield often is related to the amount of radiation intercepted by the plant canopy, absolute measurements of GLAI should have a better relationship with yield than proportional estimates of disease (stress) intensity obtained visually (Nutter et al., 1990; Nutter and Gaunt, 1996; Nutter and Littrell, 1996). The GLAI that is available to intercept radiation during the growing season is a function of the potential GLAI minus the GLAI that is reduced or removed by biotic and abiotic stresses. Therefore, temporal and spatial GLAI patterns caused by biotic and abiotic stresses can be used to help identify the cause(s) of plant stress (Dai and Khorram, 1999; Nutter, 1989; Nutter, 1990; Nutter et al., 2000). The resulting changes in GLAI due to different levels of stresses can be quantified visually as well as by remote sensing, thus facilitating the direct comparison of different methods (Nutter and Gaunt, 1996; Nutter et al., 1993).

Remote sensing offers a potential new method to correctly diagnose and quantify the actual causes of plant stress. The time of onset of plant yellowing is an important diagnostic feature. For example, symptoms caused by iron deficiency chlorosis usually appear in early June, within a few weeks of planting, whereas yellowing due to *H. glycines* typically appears in July or August, a month or two after planting. Consequently, the temporal pattern of remotely sensed images obtained over time may provide a useful means to accurately differentiate these two stresses. Thus, remote sensing coupled with GIS technologies offers new tools that may help in the early detection of *H. glycines* due to the distinctive spatial pattern (aggregations) of plant stress caused by the nematode. The use of multiple, narrow wavelength bands (measured or extracted from images) also might be used to define characteristic *H. glycines* injury spectral signatures.

The specific objectives of this research were to: (i) determine if GIS technologies can be used in conjunction with temporal, remotely sensed, and geospatially referenced data to accurately detect and quantify biotic plant stress caused by *H. glycines* in soybean fields; (ii) determine if remote sensing and GIS technologies can be used to develop methods to map plant stress in soybeans caused by *H. glycines*; and (iii) develop regression models that quantify the impact of *H. glycines* plant stress on soybean yield, soybean protein, and soy oil.

MATERIALS AND METHODS

Field experiment: *H. glycines*-susceptible soybean cultivar AgriPro 1995 was planted in a 1.2-ha SCN-infested

soybean field on 23 May 2000 at the Iowa State University Woodruff Farm near Ames, Iowa. The experimental area measured 119 × 102 m and was divided into an array of 995 2 × 3-m quadrats. Each quadrat consisted of four soybean rows (2 m wide) × 3 m in length, and plants in a 1-m-long area between the quadrats were removed to create alleys between each quadrat. The alleys helped to make the quadrats distinct for data collection (aerial and satellite images) and to facilitate the geospatial referencing of multiple types of data obtained from each quadrat.

SCN population densities: The SCN egg population density in each quadrat was assessed near the time of planting and again shortly after harvest of the soybeans. Six 2.5-cm-diam., 20-cm deep soil cores were collected from arbitrarily selected locations on either side of the two central rows of each quadrat on each sampling date. Cysts were extracted from the soil and collected on a 250-µm-pore sieve using a semi-automatic elutriator (Byrd et al., 1976). Subsequently, eggs were extracted from cysts using a stainless steel pestle and collected on a 25-µm-pore sieve (Niblack et al., 1993). Eggs were counted using a dissecting microscope.

Percentage reflectance measurements and acquisition of aerial images: Ground-based percentage reflectance measurements and aerial images were obtained simultaneously from soybean quadrats approximately every 10 to 14 days during the growing season (Table 1). Ground-based measurements were obtained using two hand-held, multispectral radiometers (CROPSCAN, Inc., Rochester, MN) between the hours of 1100 and 1500 CST (Guan and Nutter, 2001; Nutter and Gaunt, 1996). The percentage of sunlight reflected from each quadrat was measured in the near-infrared region (810 nm) from a height of 3 m above the soil line. The 810-nm wavelength band was chosen because this band was found to have the best relationship with GLAI, pathogen stress, and yield in other studies (Adcock et al., 1990; Guan and Nutter, 2000; Nutter, 1989, 1990; Nutter et al., 1999; Nutter and Littrell, 1996). Two radiometer measurements were obtained from each soy-

TABLE 1. Dates that aerial and ground-based reflectance measurements were obtained and the corresponding weather conditions.

Date	Weather
May 19	Mostly Sunny
May 22	Mostly Sunny
June 15	Partly Cloudy
June 29	Partly Cloudy
July 7	Drizzle/Mostly Cloudy
July 13	Mostly Sunny
August 2	Mostly Sunny
August 9	Partly Cloudy
August 25	Partly Sunny
September 7	Rain
September 8	Partly Sunny
September 18	Mostly Sunny

bean quadrat (one per radiometer) and averaged. In a preliminary study, reflectance measurements (individual 50-nm-wide wavelength bands from 460 to 810 nm) were related to SCN egg density, GLAI, soybean yield, soy oil, and soy protein using linear regression, and the best relationships were found using the 810-nm-wavelength band (data not shown). Thus, only the 810 nm was used in this study and only the best regression models (by date) are presented in this study.

Aerial images of the plots were taken from altitudes of 45, 55, 75, 90, 110, and 425 m during each flight. Two 35-mm single lens reflex ZX-50 Pentax cameras equipped with SMCP-FA 50 mm f/1.7 lenses (view angles 47°) were used in this study. One camera used Kodak Gold 200 daylight print film; the other used Kodak high-speed, infrared film (HIE 135-36) along with a 810-nm-wavelength filter. The cameras were inserted through a hole in the bottom of a 1978 C-152II Skyhawk aircraft. Films were commercially developed, and negatives were digitized using a Polaroid SprintScan 4000 scanner (Polaroid Corp., Cambridge, MA); all files were saved as JPEG files with zero compression.

For the aerial images (using daylight film), the red, green, and blue bands were extracted. For infrared film, only the grey levels (256) were extracted. To account for distortions for images due to atmospheric effects at high altitudes, red, green, and blue ground cloths were used to calibrate the original images (Hadjimitsis et al., 2000). Ground-based images of the cloths served as reference intensities in the red, green, and blue bands of the aerial images. Our method assumed the distribution of the distortion was homogeneous throughout the area captured by the camera. The overall color calibration scheme is shown in Figure 1.

Three correction factors for different bands were calculated as follows:

$$\text{Factor (Red Band), } F_R = \frac{I_{R,G}}{I_{R,A}}$$

$$\text{Factor (Green Band), } F_G = \frac{I_{G,G}}{I_{G,A}}$$

$$\text{Factor (Blue Band), } F_B = \frac{I_{B,G}}{I_{B,A}}$$

where

$I_{R,G}$ = Red band average intensity of ground red cloth image (scalar).

$I_{R,A}$ = Red band average intensity of aerial red cloth image (scalar).

$I_{G,G}$ = Green band average intensity of ground green cloth image (scalar).

$I_{G,A}$ = Green band average intensity of aerial green cloth image (scalar).

$I_{B,G}$ = Blue band average intensity of ground blue cloth image (scalar).

$I_{B,A}$ = Blue band average intensity of aerial blue cloth image (scalar).

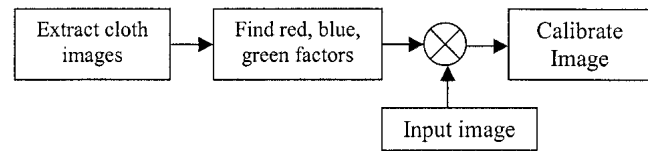


FIG. 1. Calibration scheme for correcting images due to atmospheric disturbances.

The three factors were combined into a row vector to extract three color bands from each image. These bands were combined to calculate overall image intensity: $I = [I_R \ I_G \ I_B]$, where I_R = two-dimensional matrix of red band intensity, I_G = two-dimensional matrix of green band intensity, and I_B = two-dimensional matrix of blue band intensity. Each aerial image then was corrected for color using the operation $Y = F \times I$, where Y is the corrected image.

After calibration but before selecting image intensities for comparison to the averaged radiometer readings, geometric distortions in the aerial images were corrected. The distortions were caused by the line normal to the camera not being perpendicular to the ground due to the pitch and roll of the aircraft. These corrections were made using Paint Shop Pro (Jasc Software, Inc., Eden Prairie, MN) and ArcView (ESRI, Redlands, CA) software. The tools used were the "image deformation" function in Paint Shop Pro and the "align" function in ArcView. After the distortions were corrected, quadrats were identified and geospatially referenced in the images. The quadrat regions were selected by creating a grid map using ArcView. Within each image quadrat, the red, green, and blue bands were extracted from the daylight film and the average intensity for each band was calculated. The values in each quadrat were summarized according to the grid function in ArcView found in the analysis menu. A table was created to display, label, zone code, and calculate the area, minimum, maximum, range, mean, standard deviation, and sum of the intensity for each band. The table then was exported as a database file to Microsoft Excel, and the average intensity for each band from each quadrat was geospatially referenced. The average image intensity (x) obtained from each quadrat then

TABLE 2. Landsat 7 band numbers and their corresponding spectral ranges, mid points, color spectra, and ground resolutions.

Band number	Spectral Range (nm)			Band spectrum	Ground resolution (m)
	Low	High	Mid point		
1	450	515	483	Blue	30
2	525	605	565	Green	30
3	630	690	660	Red	30
4	750	900	825	Near infrared	30
5	1,550	1,750	1,650	Mid infrared	30
6	10,400	12,500	11,450	Microwave	60
7	2,090	2,350	2,220	Far infrared	30
Pan	520	900	710	Pan	15

was regressed against the percentage reflectance measurement (y) obtained with a hand-held radiometer for each corresponding quadrat on each assessment date.

Satellite imagery: The Landsat 7 system was used to obtain satellite images of the experimental area. Landsat 7 was equipped with the Enhanced Thematic Mapper Plus (ETM+), which is an eight-band multispectral scanning radiometer. The spectral range, mid-point, and ground resolution for each Landsat 7 wavelength band is shown in Table 2. The ground sample “pixels” were 15 m in the panchromatic band; 30 m in the six visible, near infrared, and far infrared bands; and 60 m in the microwave band. Landsat 7 satellite orbits the Earth at an altitude of approximately 705 km. Its orbit is adjusted so that its 16-day repeat cycle coincides with the Landsat Worldwide Reference System. Therefore, Landsat 7 has the potential to image the same location on Earth once every 16 days. Due to flight and atmospheric conditions, Landsat 7 satellite images were acquired for only five dates during the 2000 growing season. The dates were 24 May [day of year (DOY) = 145], 9 June (DOY = 161), 27 July (DOY = 209), 12 August (DOY = 225), and 13 September (DOY = 257). The primary ground station, data handling facility, and archive facility for Landsat 7 are located at the USGS/

EROS Data Center in Sioux Falls, South Dakota. The ground system was able to distribute raw ETM+ data within 24 hours of its reception at the USGS/EROS Data Center. These scenes are available in three levels of processing—Level 0 is the raw data with no correction, Level 1R is radiometrically corrected to within 5%, and Level 1G is radiometrically corrected. This project used level 1G.

Soybean harvests and grain quality: Soybean yield data were obtained by harvesting the center two rows of each 2 × 3-m quadrat on 26 September 2000, and yield was recorded in grams per quadrat. Soybean grain was dried at 27°C for 5 days in a forced-air drier, and the grain weight (per quadrat in grams) was recorded. Soybean oil and protein concentrations for each quadrat were determined from a 100-g subsample from each quadrat using an INFRATEC 1229 grain analyzer (Tecator, Hoganas, Sweden).

Data analysis and modeling: The multispectral and digital images from the study site were processed, classified, and analyzed by the ERDAS IMAGINE (ERDAS, Inc., GA) and ENVI (Research Systems Inc., Boulder, CO) software programs in conjunction with ArcView GIS and Spatial Analysts software (ESRI, Redlands, CA). Each image layer (satellite, aircraft, hand-held ra-

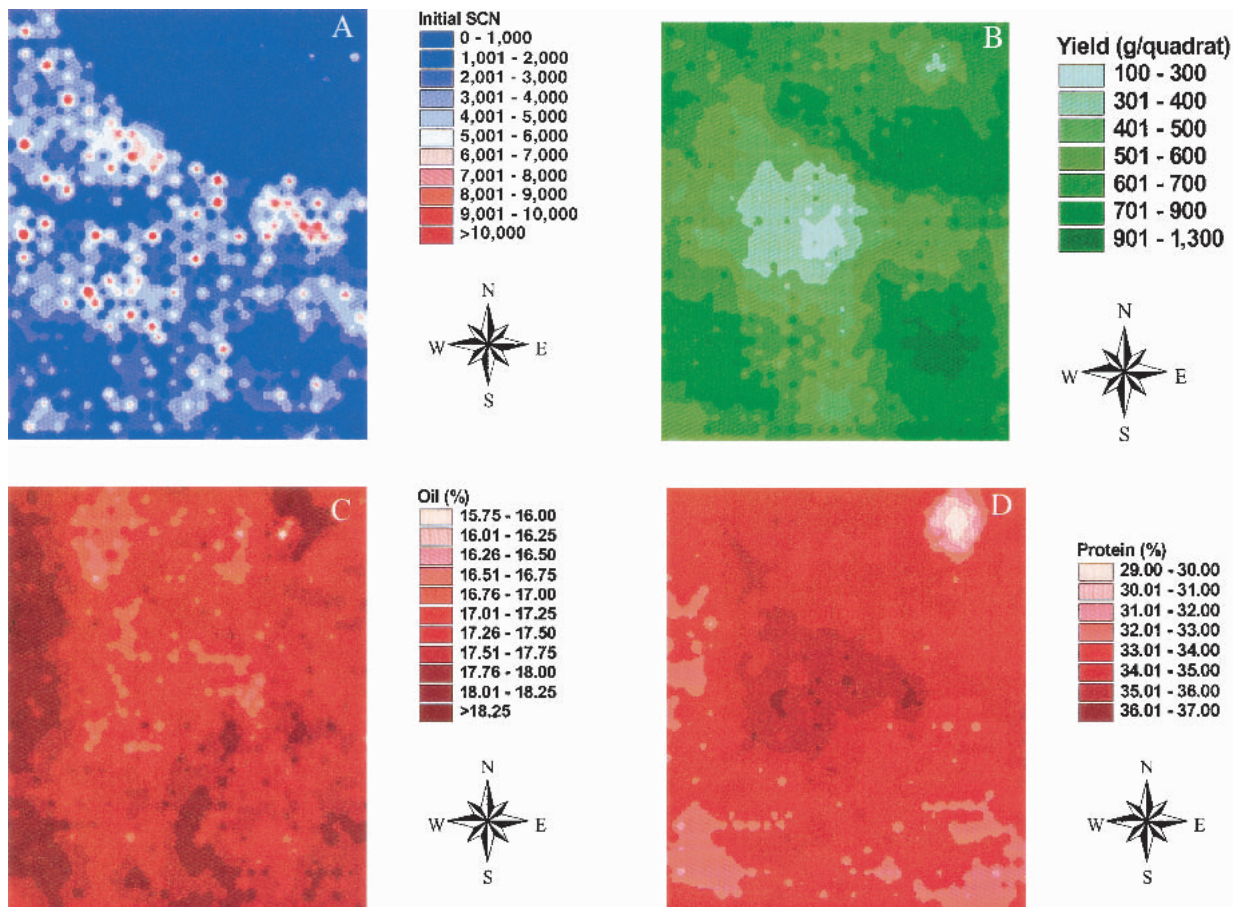


FIG. 2. Map of (A) initial soybean cyst nematode population densities, (B) soybean yield, (C) soy oil, and (D) soy protein concentration for a 1.2-ha soybean field at the Woodruff farm, Ames, Iowa, in 2000. The dimension of the field is 102 × 119 m.

diameter) and ground truth measurements of plant stresses and crop information (nematode population densities and GLAI) were geospatially referenced using GPS and GIS technologies. Images were rectified using ArcView software, processed, and then combined and analyzed by producing overlay maps for each platform level (scale). Spatial analyses of data collected in the study were conducted using SAS (SAS Institute, Inc., Cary, NC) and S-Plus (Mathsoft, Seattle, WA) statistical analysis software and XGobi (Iowa State University, Ames, IA) advanced data visualization environment. Both S-Plus and XGobi provide analytical environments for data visualization and data mining. Image analysis of Landsat scenes were accomplished using IMAGINE software from ERDAS.

Linear regression was used to quantify the relationships among the different remote sensing platforms and their effects on image characteristics with respect to known levels of biotic and abiotic plant stresses.

Maps depicting within-field variations in initial SCN population densities, yield, soy oil, and soy protein were developed using the GIS software program ArcView.

RESULTS

GIS field maps: Using the GIS software program ArcView, spatial maps depicting quantitative information concerning initial SCN population densities (Fig. 2A), soybean yield (Fig. 2B), soy oil (Fig. 2C), and soy protein concentration (Fig. 2D) were developed. Initial SCN population densities ranged from zero to >10,000/100 cm³ soil, while soybean yields ranged from 175.9 to 1,138.9 g/quadrat (586.3 to 3,796.3 kg/ha). Within-field soy oil concentrations ranged from 15.9% to 18.6%, whereas soy protein concentrations ranged from 29.0% to 37.0%.

Ground-based percentage reflectance measurements: Percentage reflectance measurements (810 nm) (DOY

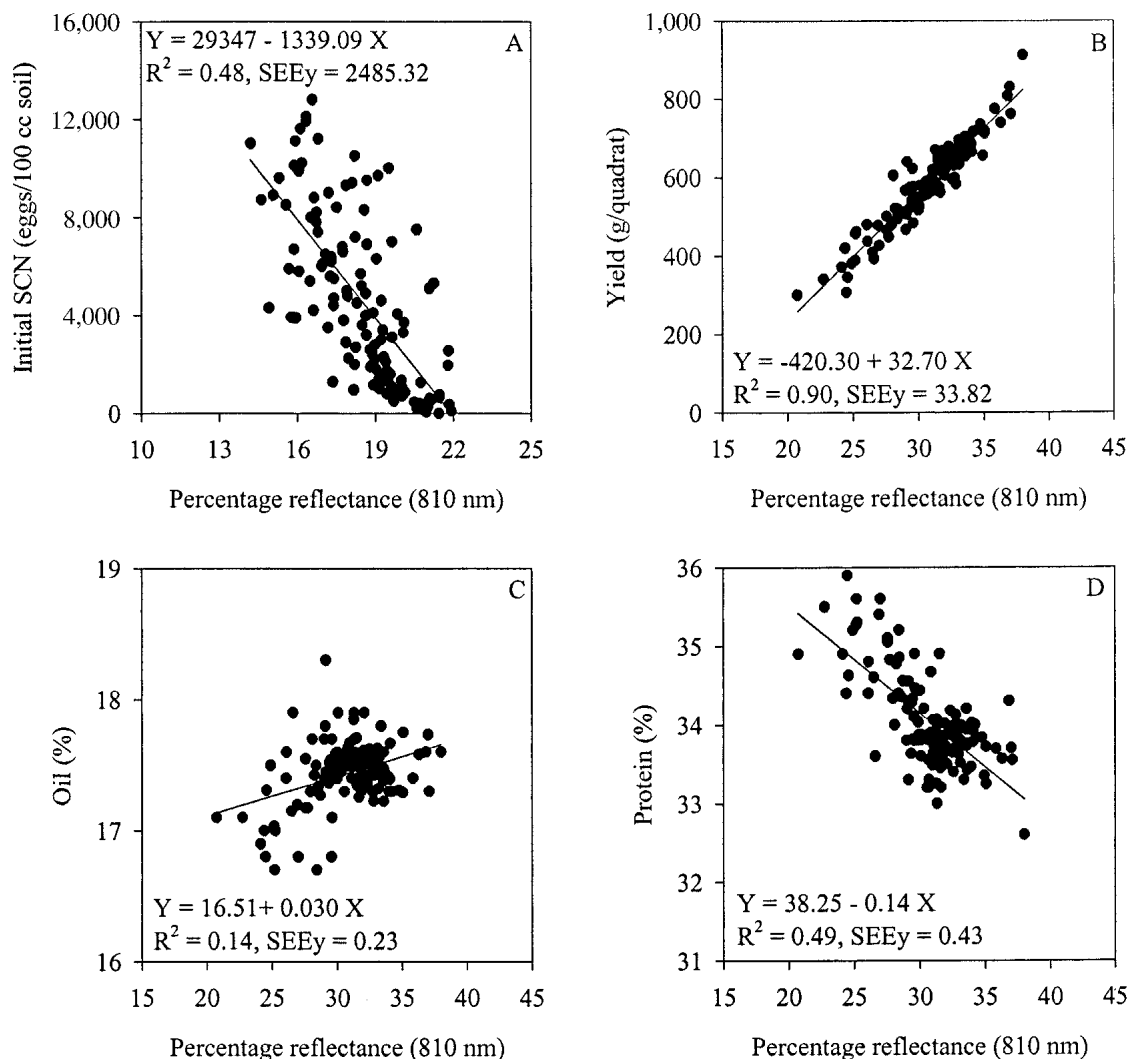


FIG. 3. Relationship between percentage reflectance (810 nm) and (A) initial soybean cyst nematode population density on 13 July (DOY 195), (B) soybean yield on 25 August (DOY 238), (C) soy oil on 25 August (DOY 238), and (D) soy protein on 25 August (DOY 238) for a 1.2-ha soybean field at the Woodruff farm, Ames, Iowa, in 2000.

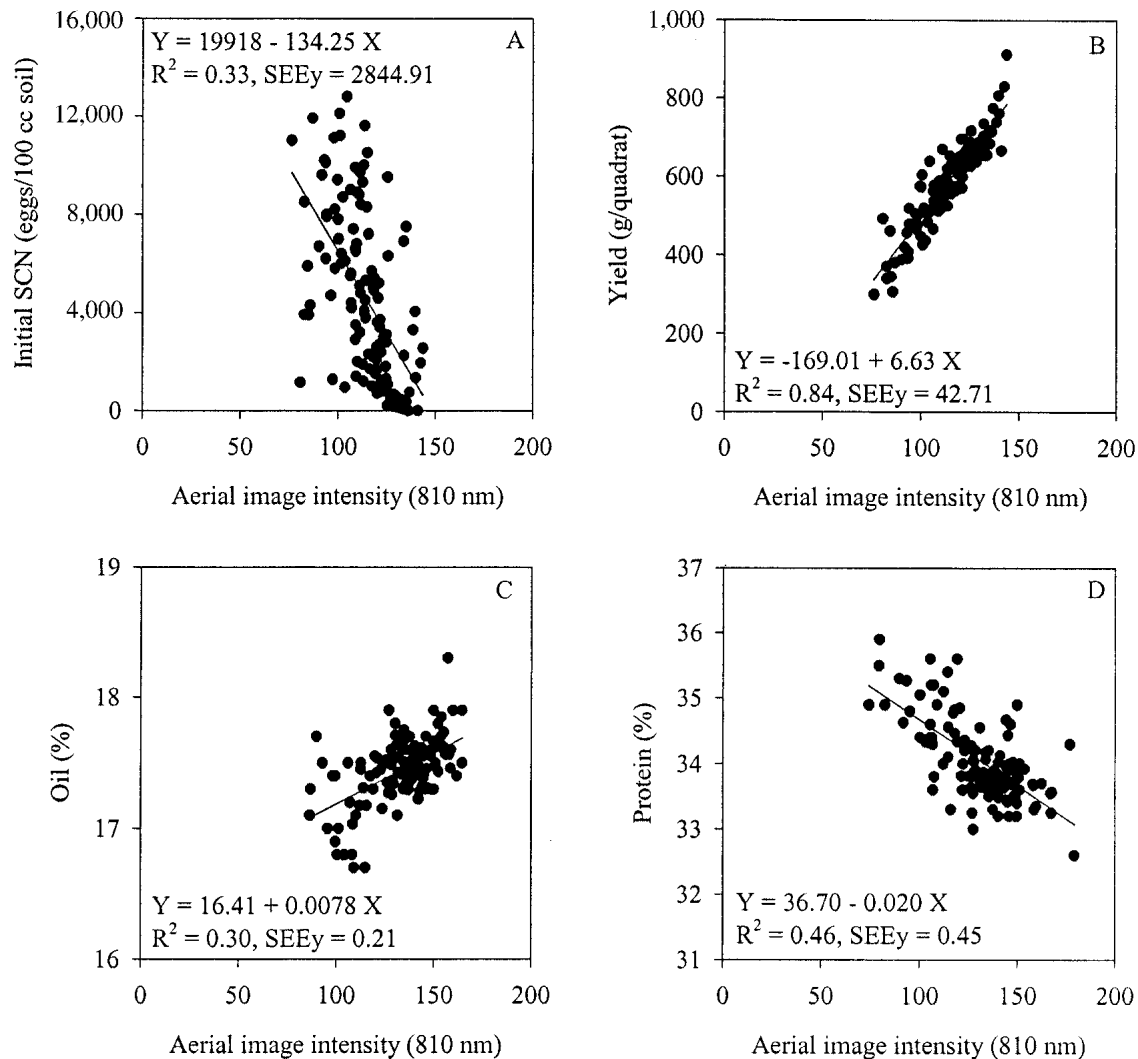


FIG. 4. Relationships between aerial photo image intensities (810 nm) on 8 September (DOY 252) and (A) initial soybean cyst nematode population density, (B) soybean yield on 8 September (DOY 252), (C) soy oil on 7 September (DOY 251), and (D) soy protein on 25 August (DOY 238) at the Woodruff farm, Ames, Iowa, in 2000. Aerial images were obtained at a height of 425 m.

238) explained 48%, 90%, 14%, and 49% of the variation in initial SCN population density, soybean yield, soy oil concentration (%), and soy protein concentration (%), respectively (Fig. 3A–D). Percentage reflectance at 810 nm had the best relationship with SCN population density on 13 July (DOY 195). As percentage reflectance values increased, initial SCN population densities (Fig. 3A) and protein concentrations (Fig. 3D) decreased, while both soybean yield (Fig. 3B) and soybean oil concentration (Fig. 3C) increased as percentage reflectance values increased. This indicates that as plant stress increases, percentage reflectance at 810 nm decreases (i.e., the higher the reflectance the lower the stress, the higher the soybean yield and soy oil concentration, and the lower the soy protein concentration). Other researchers also have reported higher disease stress in soybeans resulted in higher protein levels in harvested grain (Steinlage *et al.*, 2002).

Aerial images: Aerial image intensity values (810 nm)

explained up to 33, 84, 30, and 46% of the variation in initial SCN population density, soybean yield, soy oil concentration, and soybean protein concentration, respectively (Fig. 4A–D). When aerial image intensity was regressed with initial SCN population density and soy protein concentration, negative linear relationships were detected (Fig. 4A and 4D, respectively). Positive linear relationships were found, however, when aerial image intensity was regressed against soybean yield and soy oil concentration (Fig. 4B and 4C, respectively).

Satellite imagery: Because the resolution of Landsat 7 imagery ranged from 15 to 60 m, this resulted in only 16 data points (larger soybean plots created by averaging over quadrats) for each regression analysis. Due to averaging, SCN initial population densities in these 16 plots ranged from 516 to 3,472 eggs/100 cc soil, and soybean yields ranged from 414.6 to 816.2 g/plot (Fig. 5A, B). In spite of averaging over quadrats to produce larger soybean plots, there was a good linear (negative)

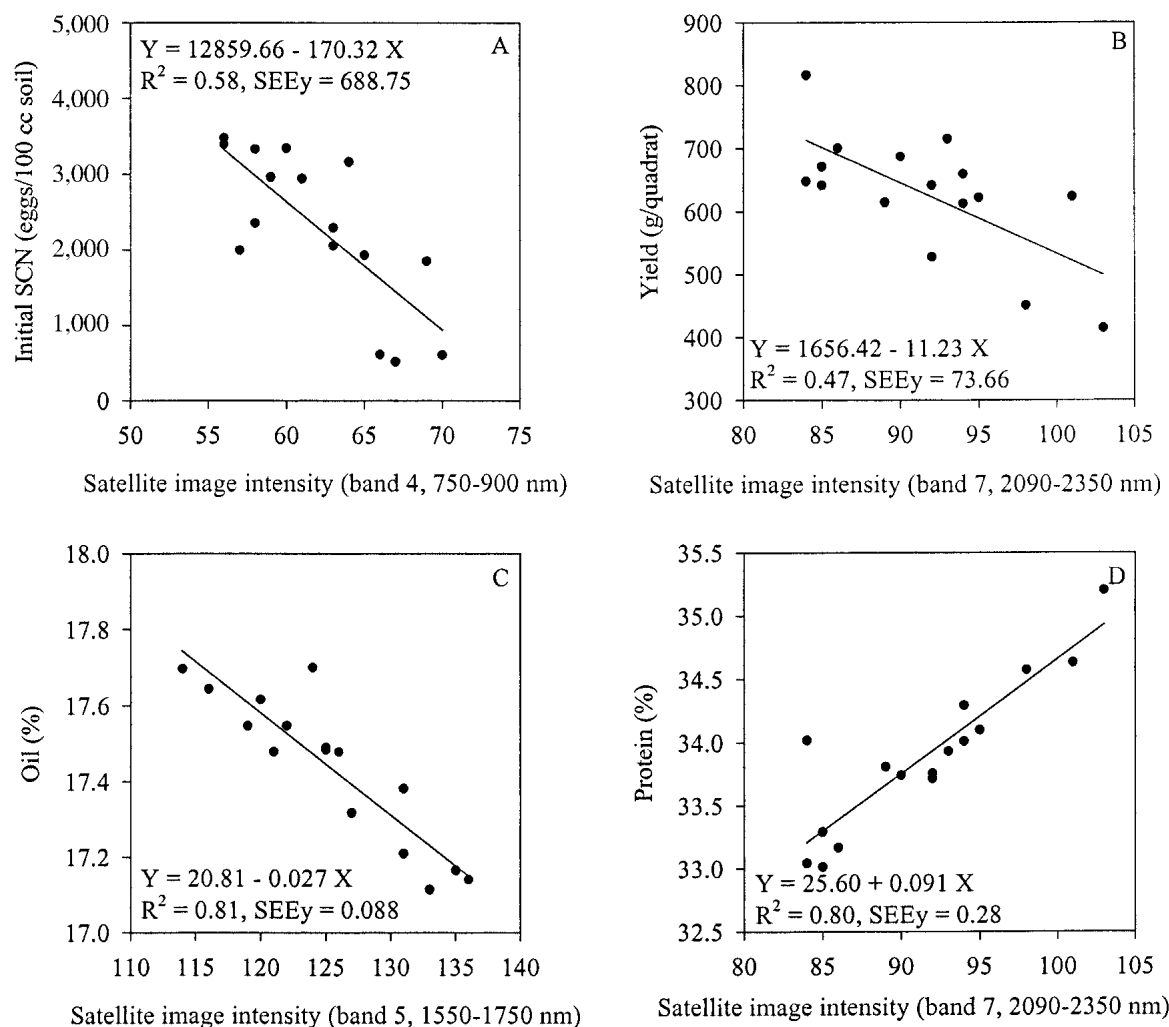


FIG. 5. Relationships between satellite image intensities and (A) initial soybean cyst nematode population density, (B) soybean yield, (C) soy oil, and (D) soy protein at the Woodruff farm, Ames, Iowa, on 13 September 2000.

relationship between satellite image intensity (band 4, 750–900 nm) and SCN initial population density and satellite image intensity (band 7, 2,090–2,350 nm) and soybean yield (Fig. 5A and 5B, respectively). **Satellite image intensity explained more of the variation in initial SCN population density ($R^2 = 0.58$) compared to either aerial image intensity ($R^2 = 0.33$) (Fig. 4A) or ground-based, percentage reflectance measurements ($R^2 = 0.48$) (Fig. 3A).**

Satellite image intensity also explained more of the variation in soybean oil concentration ($R^2 = 0.81$) (Fig. 5C) and soybean protein concentration ($R^2 = 0.80$) compared to aerial and ground-based measurements. Soy oil (%) decreased as satellite image intensity (band 5) increased, whereas soy protein concentration increased as satellite image intensity increased (Fig. 5C and 5D, respectively).

Temporal reflectance pattern: The difference in the percentage reflectance (810 nm) between soybean quadrats with high initial SCN population densities (>10,000 eggs/100 cc soil) vs. quadrats where SCN eggs

were not detected revealed a distinct temporal pattern (Fig. 6). The greatest difference in percentage reflectance over time at 810 nm was observed on day of year (DOT) 225 (2 August 2000).

Relationship between ground-based and aerial-based remote sensing data: Mid to late in the 2000 growing season, aerial-based image intensities explained 10% to 95% of the variation in ground-based percentage reflectance (810 nm) values (Fig. 7). The best relationship between aerial image intensity (x) and ground-based percentage reflectance measurements (y) was found on 8 September 2000 (DOY 258). Percentage reflectance (810 nm) increased by 0.16% for each 1% increase in aerial image intensity ($R^2 = 0.95$, $SEE_y = 0.58$) (Fig. 8).

Relationships with soybean yield: **All three remote sensing platforms (ground-based, aerial, and satellite) explained more of the variation in yield than the more traditional method that relies on quantifying initial SCN populations (eggs/100 cm³ soil) and regressing these data with respect to yield. Using the traditional method, SCN population density explained only 31%**

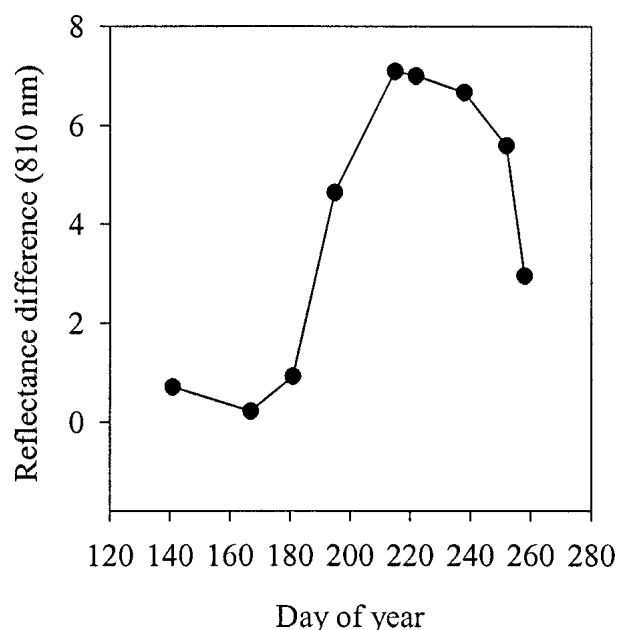


FIG. 6. Temporal pattern concerning the difference in percentage reflectance at 810 nm between soybean quadrats with high SCN population densities (>8,900 eggs/100 cc soil) and soybean quadrats where SCN eggs were not detected, at the Woodruff farm, Ames, Iowa, 2000.

of the variation in soybean yield among quadrats (Fig. 9), while ground-based, aerial, and satellite measurements explained 90%, 84%, and 47% of the variation in soybean yield, respectively (Figs. 3B, 4B, and 5B, respectively).

DISCUSSION

Heterodera glycines is a widespread and serious pest of soybeans throughout the United States, yet many in-

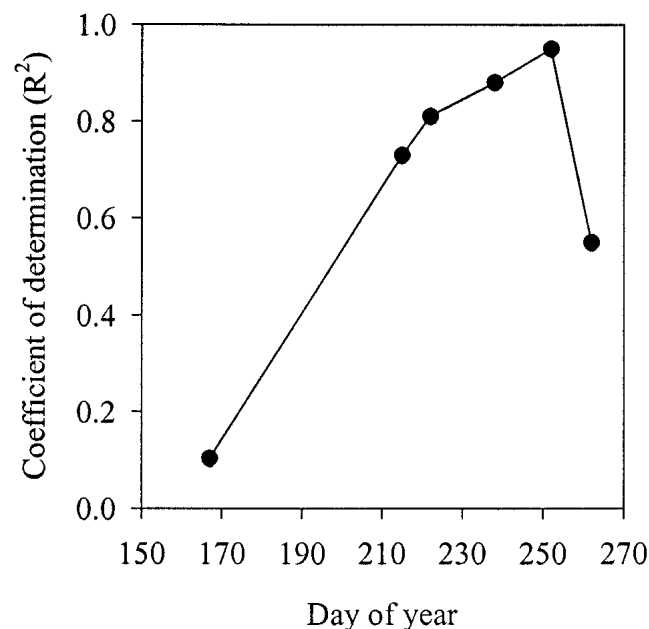


FIG. 7. Coefficients of determination vs. day of year for linear regression between percentage reflectance (810 nm) obtained using radiometers and aerial photo image intensities at Woodruff farm in Ames, Iowa, 2000.

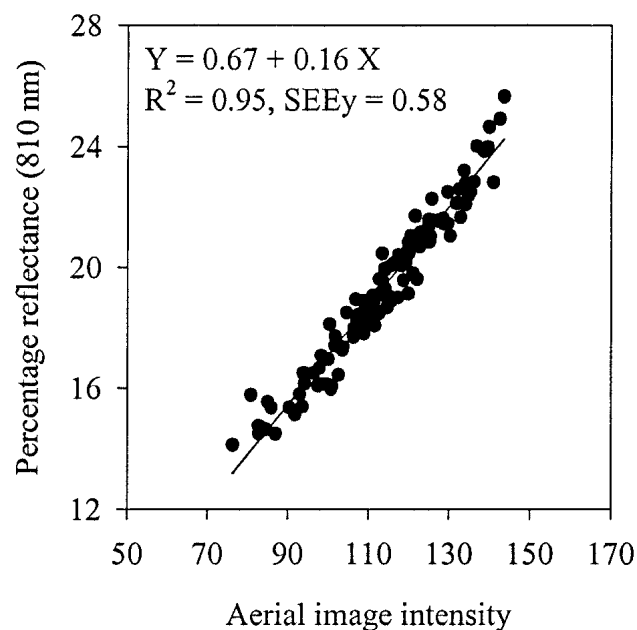


FIG. 8. Relationship between aerial image intensity (810 nm) and percentage reflectance (810 nm) on 8 September 2000 (DOY 252) at Woodruff farm, Ames, Iowa, 2000.

festated fields are not known to be infested by those who farm the land. The lack of awareness of infestations by growers results in the buildup of the nematode to very high population densities that eventually cause catastrophic crop losses. One reason that fields are not routinely checked for the presence of *H. glycines* is the cost of sampling fields. Clearly, development of a means for remote detection of *H. glycines* infestations (for example, via aerial images) would reduce the costs associated with the scouting of fields for this pest. Conse-

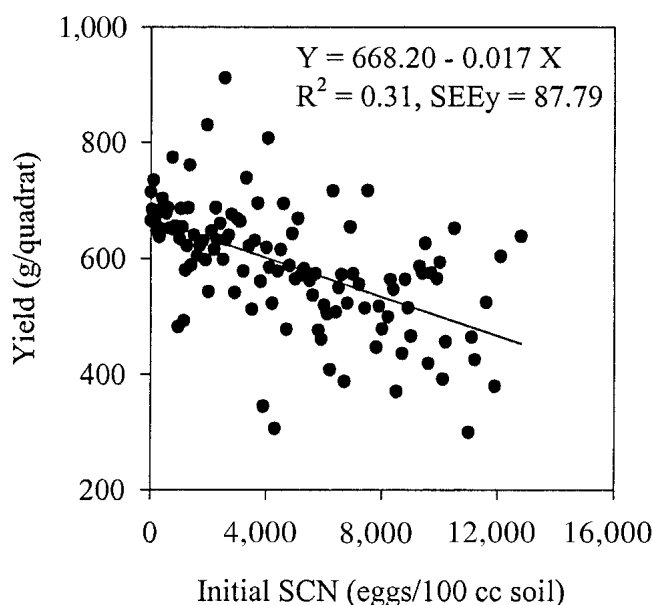


FIG. 9. Relationship between initial SCN population density (eggs/100 cc soil) and soybean yield at Woodruff farm, Ames, Iowa, 2000.

quently, growers would be more likely to check fields for the presence of *H. glycines* on a routine basis and *H. glycines* infestations would be discovered earlier and at lower population densities; thus, management of the nematode would begin sooner, resulting in higher soybean yields than would be achieved if *H. glycines* infestations were allowed to increase unchecked.

This research describes work in progress to identify soybean fields that are infested with *H. glycines* based on reflectance and image intensity patterns of *H. glycines*-infected soybean canopies. Based on our results, remote sensing and GIS technologies could soon become invaluable tools for alerting soybean growers when and where to check their fields for the presence of *H. glycines*. Such remote sensing also may prove valuable in monitoring the performance of SCN-resistant soybean varieties for loss of effectiveness due to directional selection of SCN populations that can successfully reproduce on resistant soybean varieties. Currently, assessments of plant health and productivity are conducted using field scouting, ground-based soil sampling, and costly SCN testing methods. These scouting, sampling, and testing methods are extremely time and labor intensive, particularly when the crop area to be assessed is large.

A unique aspect of this project was that remote sensing data were collected simultaneously from satellite, aircraft, and ground-based, multispectral radiometer. This methodology allowed us to make appropriate calibrations for different atmospheric conditions. By simultaneously collecting data from these different platforms, we could quantitatively determine the trade-offs among the different remote sensing platforms and the quality of the data in assessing soybean health and predicting soybean yield. For example, there were significant linear relationships between aerial image intensities and ground-based radiometer readings in the infrared region, yet aerial imaging has the advantage of being able to monitor larger areas than the ground-based reflectance method. Significant relationships also were found between image intensities and soybean yield and SCN population densities.

A key to effective decision making in precision agriculture is the ability to obtain remotely sensed images that clearly depict the spatial and temporal pattern of plant stress at a resolution that allows the farm producer and (or) crop consultant to cost effectively deploy a crop management tactic. Our results suggest that aerial images can replace ground-based radiometers to efficiently assess the health and productivity of soybean fields. The methods we have developed might help farmers identify which parts of the fields might be infested with SCN, thereby allowing for immediate action and precautions to be taken to avoid spread of SCN. The distinctive temporal pattern in the difference in reflectance values from quadrats with high vs. low nematode population densities may be unique to stress

caused by SCN and could provide an important diagnostic tool when attempting to determine the causes of crop stress in soybeans.

Our ultimate goal is to develop methodologies to provide timely assessments concerning the health and productivity for regional cropping areas as well as for individual fields. The combination of remotely sensed data from different remote sensing platforms (ground, aircraft, satellite), coupled with the use of GIS and Global Positioning System (GPS) technologies and sophisticated data analysis tools, will benefit precision agriculture by providing growers and their consultants with cost-effective and timely techniques to diagnose and quantify the causes of plant stress in soybean fields. This project, which has tremendous relevance to USDA and NASA missions in providing information to better help farmers manage their crops, integrates and uses remote sensing, GPS, and GIS technologies to facilitate the generation and delivery of timely, reliable, and cost-effective disease/crop management information.

Integrating remote sensing technologies into the day-to-day management of cropping systems (precision agriculture) offers tremendous new opportunities for farmers to cost effectively narrow the yield gaps that currently constrain agricultural cropping systems worldwide. Yield gaps are defined as the potential yields that growers could achieve for specific fields if plant stress were alleviated, minus the yields they actually harvest (Nutter et al., 1993; Nutter and Littrell, 1996). Remote sensing, GIS, and GPS technologies have the potential to revolutionize the way in which farmers manage their crops (Anderson et al., 1999); however, key conceptual and quantitative links concerning the relationships between remote sensing data and biological systems are often lacking. To fully maximize the management/yield benefits that might be achieved by integrating GIS, GPS, and remote sensing technologies into disease management programs, it is first necessary to: (i) accurately differentiate vegetation types (crops, natural vegetation, forests, etc.), (ii) recognize when soybean plants (fields) are stressed, (iii) accurately determine what is causing plant stress, (iv) quantify the degree of plant stress within fields, (v) quantify and relate remote sensing assessments for plant stress with ground truth (visual) assessments for plant health and crop/plant productivity (yield, oil, protein, fiber), and (vi) develop crop stress thresholds for plant populations that alert the farmer (in a timely manner) when available soybean stress mitigation measures should be deployed to optimize the farmer's net return on investment. Additional research is needed in all six areas.

LITERATURE CITED

- Adcock, T. E., F. W. Nutter, Jr., and P. A. Banks. 1990. Measuring herbicide injury to soybeans (*Glycine max*) using a radiometer. *Weed Science* 38:625-627.
- Anderson, J. E., R. L. Fischer, and S. R. Deloach. 1999. Remote

sensing and precision agriculture: Ready for harvest or still maturing? *Photogrammetric Engineering Remote Sensing* 10:1118–1123.

Byrd, D. W., Jr., K. R. Barker, H. Ferris, C. J. Nusbaum, W. E. Griffin, R. H. Small, and C. A. Stone. 1976. Two semi-automatic elutriators for extracting nematodes and certain fungi from soil. *Journal of Nematology* 8:206–212.

Dai, L. X., and S. Khorram. Remotely sensed change detection based on artificial neural networks. *Photogrammetric Engineering Remote Sensing* 10:1187–1194.

Faivre, R., and A. Fischer. 1996. Predicting crop reflectances using satellite data observing mixed pixels. *Journal of Agricultural, Biological, and Environmental Statistics* 2:87–107.

Guan, J., and F. W. Nutter, Jr. 2000. Relationships between defoliation, leaf area index, canopy reflectance, and forage yield in the alfalfa leaf spot pathosystem. Pp. 319–326 *in* Second International Conference on Geospatial Information in Agriculture and Forestry, ERIM International, Inc., Ann Arbor, MI.

Guan, J., and F. W. Nutter, Jr. 2001. Factors affecting the quality and quantity of sunlight reflected from alfalfa canopies. *Plant Disease* 85:865–874.

Hadjimitsis, D. G., D. R. I. Clayton, V. S. Hope. 2000. Pp. 194–201 *in* The Importance of Accounting Atmospheric Effects in Satellite Remote Sensing: A Case Study from the Lower Thames Valley Area, UK, Reston, VA, Space 2000, American Society of Civil Engineers.

Jackson, R. D., C. A. Jones, G. Uehara, and L. T. Santo. 1980. Remote detection of nutrient and water deficiencies in sugarcane under variable cloudiness. *Remote Sensing of Environment* 11:327–331.

Niblack, T. L., R. D. Heinz, G. S. Smith, and P. A. Donald. 1993. Distribution, density, and diversity of *Heterodera glycines* in Missouri. Supplement to the *Journal of Nematology* 25:880–886.

Nutter, F. W., Jr. 1989. Detection and measurement of plant disease gradients in peanut with a multispectral radiometer. *Phytopathology* 79:958–963.

Nutter, F. W., Jr. 1990. Remote sensing and image analysis for crop

loss assessment. Pp. 93–105 *in* Crop Loss Assessment in Rice. Los Banos, Philippines, International Rice Research Institute.

Nutter, F. W., Jr., and R. E. Gaunt. 1996. Recent developments in methods for assessing disease losses in forage/pasture crops. Pp. 93–118 *in* Pasture and Forage Crop Pathology. Madison, WI. American Society of Agronomy, Inc., Crop Science Society of America, Inc., Soil Science Society of America, Inc.

Nutter, F. W., Jr., J. Guan, and R. J. Percifield. 2000. Assessing crop health in time and space by measuring spectral reflectance of solar radiation from plant canopies. Pp. 165–176 *in* Second International Conference on Geospatial Information in Agriculture and Forestry, ERIM, International, Inc., Ann Arbor, MI.

Nutter, F. W., Jr., J. Guan, R. J. Percifield, B. Menelas, T. R. Rosburg, S. Bidney, J. P. Basart, C. S. Chong, M. Cook. 1999. Use of remote sensing to quantify the impact of plant disease epidemics on plant biomass and productivity. Ninth Annual Space Grant Conference, 5 November, University of Northern Iowa, Cedar Falls, IA.

Nutter, F. W., Jr., and R. H. Littrell. 1996. Relationships between defoliation, canopy reflectance, and pod yield in the peanut-late spot pathosystem. *Crop Protection* 15:135–142.

Nutter, F. W., Jr., R. H. Littrell, and T. B. Brenneman. 1990. Utilization of a multispectral radiometer to evaluate fungicide efficacy to control late leaf spot in peanut. *Phytopathology* 80:102–108.

Nutter, F. W., Jr., P. S. Teng, and M. H. Royer. 1993. Terms and concepts for yield, crop loss, and disease thresholds. *Plant Disease* 77:211–215.

Steinlage, T. A., J. H. Hill, and F. W. Nutter, Jr. 2002. Temporal and spatial spread of *soybean mosaic virus* (SMV) in soybeans transformed with the coat protein gene of SMV. *Phytopathology* 92:478–486.

Workneh, F., G. L. Tylka, X. B. Yang, J. Faghihi, and J. M. Ferris. 1999. Assessment of soybean brown stem rot, *Phytophthora sojae*, and *Heterodera glycines* in the north-central United States using area-frame sampling: Prevalence and effects of tillage. *Phytopathology* 89:204–211.